# Direct MOCVD Growth of Iron Oxide on Three-Dimensional Nickel Foam as Electrode for the Oxygen Evolution Reaction

Christian Stienen[a] and Georg Bendt*[a]

Iron oxide thin films were grown directly on three-dimensional nickel foam via metalorganic chemical vapor deposition (MOCVD) in the temperature range of 250–450 °C using $Fe(CO)_5$ as precursor. Iron oxide ($\alpha$-$Fe_2O_3$) films were formed at low substrate temperatures (250–350 °C), whereas the additional growth of an underlying NiO film occurred at substrate temperatures above 350 °C. The electrochemical activities of the as-formed binder-free and noble metal-free electrodes were tested for the oxygen evolution reaction (OER) in alkaline media. An overpotential reduced by 250 mV at a current density of 50 mA cm$^{-2}$ and a lower Tafel slope of 55 mV dec$^{-1}$ compared to bare nickel foam were found for the best-performing electrocatalyst, while the long-term stability of the as-formed electrodes was proven by chronopotentiometry. The surface morphology of the iron oxide films was characterized by scanning electron microscopy, whereas the crystallographic phase as well as the elemental composition were determined by X-ray diffraction, energy-dispersive X-ray spectroscopy, X-ray photoelectron spectroscopy, and time-of-flight secondary ion mass spectrometry in the pre- and the post-catalytic state.

## Introduction

The electrochemical water splitting reaction is well known since the early days of chemistry.[1] In fact, it is likely to become an important cornerstone of a modern energy grid as it allows the easy synthesis of hydrogen as a storable and transportable energy carrier.[2] With most of the existing electrode materials, the broad application of this technique is currently limited by the high overvoltage required for the oxygen evolution reaction (OER) in order to overcome the sluggish reaction kinetics. In this case, the required overpotential is significantly higher than the theoretical minimum threshold voltage of 1.23 V. The interest in highly active yet stable electrocatalysts that can withstand the harsh conditions of OER has prompted widespread investigations on the use of nanoparticles,[3] often cobalt-based (e.g., layered double hydroxides,[4] oxides,[5] phosphides,[6] or sulfides[7]) on glassy carbon or nickel foam electrodes. Unfortunately, cobalt is a toxic element that can easily leach out under the conditions of the OER,[8] and despite being non-abundant, cobalt is still used in large quantities for the purpose of electrochemical energy storage. Consequently, an ideal electrocatalyst should be free of precious metals, non-toxic, inexpensive, highly active, and show long-term stability under OER conditions. Iron oxides, for example, are highly abundant in nature and can be found in various modifications. Yet, despite meeting several important criteria of a potential OER catalyst, little research has been done on pure iron oxides mainly due to their poor electronic conductivity, which could ultimately compromise their electrochemical activity. Hollow nanorods of pure $Fe_2O_3$, for instance, which were prepared via co-precipitation, showed very low OER activity, whereas a composite material containing oxidized multi-walled carbon nanotubes showed enhanced catalytic activity.[9] Although iron oxides are also not well investigated in electrochemical water splitting reactions, hematite ($\alpha$-$Fe_2O_3$) makes a promising photoanode material for photoelectrocatalytic water splitting.[10] Nickel-containing iron compounds were also studied as better alternatives to pure iron oxides. Here, Liu et al reported on the hydrothermal growth of spinel $NiFe_2O_4$ in the form of nanospindle arrays on $FeNi_3$ foam, which were successfully applied as electrodes for the OER.[11] Moreover, $NiFe_2O_4$ was investigated as a bifunctional electrocatalyst for OER and hydrogen evolution reaction (HER) in alkaline medium.[12] In addition to oxides, iron nickel layered double hydroxides ($FeNiO_xH_y$) have been identified as highly active electrocatalysts for the OER.[13]

Unfortunately, nanoparticles have several disadvantages, one of which is that they must be immobilized and electrically connected to the electrode surface. Such a process typically requires the use of a binder, a conductive polymer (e.g., Nafion), and/or a carbon support (carbon black, Vulcan, carbon nanotubes) that simultaneously buries a part of the particles. The effect of the binder on the electrochemical activity is currently under discussion; however, common problems include the time-consuming fabrication of the electrode, the high contact resistivities between the particles and the support, and the tendency of the electrochemically active layer to peel off

[a] C. Stienen, Dr. G. Bendt
University Duisburg-Essen
Institute for Inorganic Chemistry and Center for Nanointegration Duisburg-Essen (Cenide)
Universitätsstraße 5–7, 45117 Essen (Germany)
E-mail: georg.bendt@uni-due.de

Supporting information for this article is available on the WWW under https://doi.org/10.1002/cssc.202001896

after long times of operation. Furthermore, an upscaling of the electrode manufacturing is not straightforward, and hence this method remains unfavorable for industrial use. However, recent approaches that involve the direct growth of electrochemical active materials on electrodes under hydrothermal conditions became widely employed to avoid the problems associated with organic binders.[14] To the best of our knowledge, the direct (metalorganic) chemical vapor deposition [(MO)CVD] of an OER electrocatalyst has rarely been reported. Several of the reported synthetic protocols include a one-step gas-phase process in a multi-step procedure. Sagu et al. described the growth of $CoFe_2O_4$ on fluorine-doped tin oxide (FTO) glass using an aerosol-assisted CVD process (AACVD) by reacting a precursor solution of iron(III) acetylacetonate and cobalt(II) acetate in methanol at a substrate temperature of 500 °C.[15] The resulting $CoFe_2O_4$ film showed an overpotential of 490 mV at 10 mA $cm^{-2}$ current density and a Tafel slope of 54.2 mV $dec^{-1}$ for the OER in alkaline media. Weidler et al. reported on the MOCVD growth of $CoO_x$ thin films using $Co(acac)_3$, as well as the growth of the oxide $NiO_x$, the oxyhydroxides $NiO_x(OH)_y$, and $CoNiO_x(OH)_y$ from $Co(acac)_3$ and $Ni(acac)_2$ using a plasma-enhanced CVD process (PECVD) on titanium substrates.[16]

We herein report on our attempts to grow iron oxide directly on nickel foam as an electrochemical active layer via MOCVD. Their potential as electrode for the OER in alkaline media will be discussed.

## Results and Discussion

### Pre-OER characterization

MOCVD deposition studies were performed at different substrate temperatures ranging from 250 to 450 °C. For reasons of clarity, the samples are referred as $Fe_2O_3$@Ni-XXX (Ni foam substrate) or $Fe_2O_3$@NiF-XXX (Ni foil substrate), where XXX indicates the deposition temperature. In all deposition experiments, a reddish-brown film was formed on the Ni substrate.

Figure 1b,c displays low-magnification scanning electron microscopy (SEM) photographs of an iron oxide film deposited at 300 °C on Ni foam. The SEM image reveals a closed film without holes or cracks on the nickel surface. The visible micrometer-sized grains originate from the nickel foam. The SEM photograph of higher magnification shows that the film consists of densely packed and uniform nanosized (30–100 nm) grains. The granular surface morphology is also visible in the atomic force microscopy (AFM) image (Figure 1d, Figure S3). Our SEM studies reveal that the substrate temperature has hardly any influence on the film morphology and the grain size. (Supporting Information, Figures S1–S6). The chemical composition of the material film was analyzed by energy-dispersive X-ray spectroscopy (EDX; Supporting Information, Figures S17–S21), showing the expected signals for oxygen (O–$K_\alpha$ =

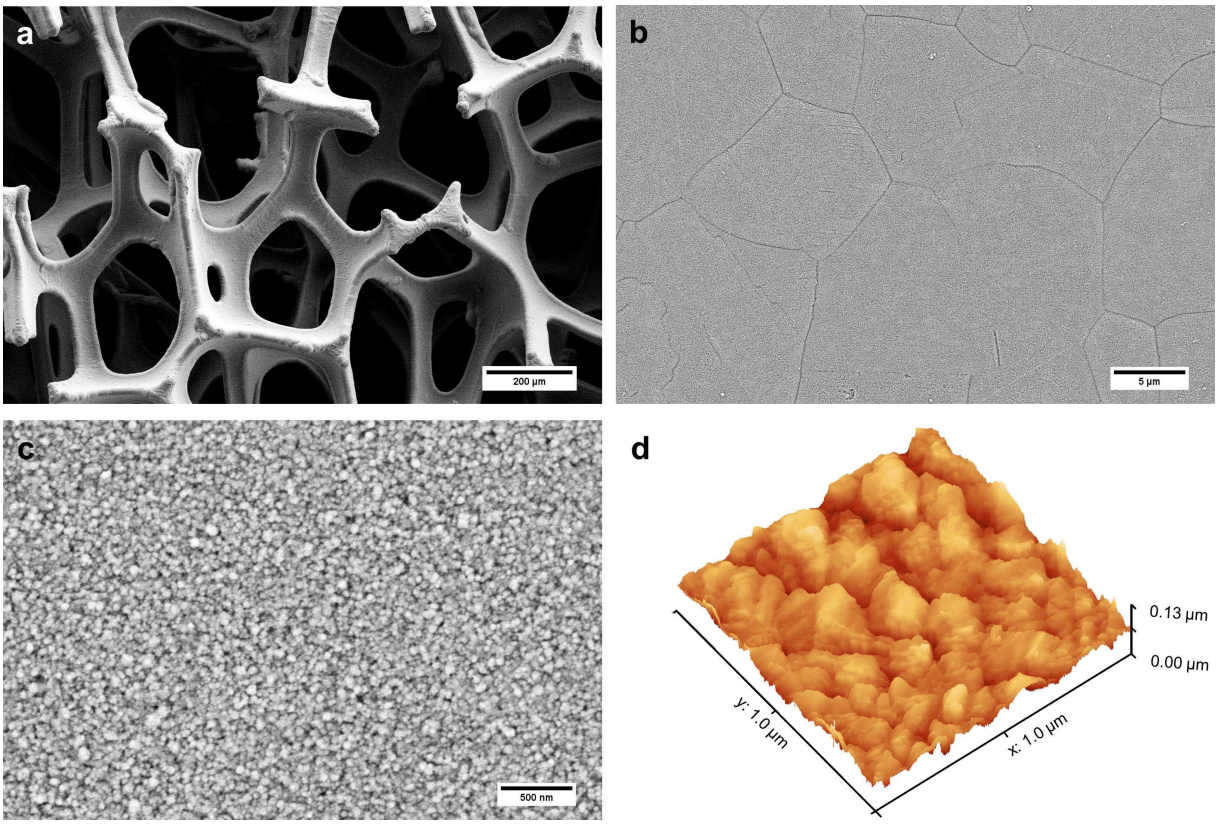


**Figure 1.** Representative low- and high-magnification SEM (a–c) and AFM images (d) of a film grown on Ni foam at a substrate temperature of 300 C. Scale bars: 200 µm (a), 5 µm (b), 500 nm (c).

0.525 keV), iron (Fe–$K_\alpha$ = 6.398 keV), and nickel (Ni–$K_\alpha$ = 7.471 keV) from the substrate.

The X-ray diffraction (XRD) patterns of iron oxide films deposited at different substrate temperatures are displayed in Figure 2a. The film deposited at 250 °C shows no Bragg reflections, which indicates a largely amorphous film. At higher substrate temperature of 300 °C, the formation of crystalline hematite $\alpha$-$Fe_2O_3$ can be observed from the characteristic reflexes at 24.2, 33.1, and 35.7°. The reflections are broadened due to the nanosized nature of the $\alpha$-$Fe_2O_3$ grains in the film. The reflections become sharper and more intense with increasing deposition temperature of 350 °C. At 400 °C, $\alpha$-$Fe_2O_3$ is no longer present as a crystalline phase, instead the formation of the rock salt-type NiO phase is observed. This phase was identified by a reflex at 37.25° since the other expected reflexes are masked by the intense signals of the nickel substrate. The measured value for the reflex position is not shifted compared to the literature value (37.28°), hence the incorporation of iron in the NiO lattice can be excluded. The absence of crystalline $\alpha$-$Fe_2O_3$ in the XRD pattern is a result of the decreasing film thickness with increasing substrate temperature due to the etching process and premature decomposition of the temperature sensitive iron precursor. As for the $\alpha$-$Fe_2O_3$ phase, the NiO reflex becomes sharper and more pronounced with increasing temperature.

Figure 2b shows the Raman spectra of the MOCVD grown films prepared at different substrate temperatures. The iron oxide deposited at 300 and 350 °C on Ni foam was identified by XRD as $\alpha$-$Fe_2O_3$. The $\alpha$-$Fe_2O_3$ crystallizes in the trigonal *R*-3*c* crystal space group and with seven phonon modes; two $A_{1g}$ phonon modes and five $E_g$ phonon modes are expected.[17] The signal with the lowest frequency of 225.7 $cm^{-1}$ can be assigned to $A_{1g}$ mode, while the bands at 254.3, 291.5, 299.6, 410.7, and 610.1 $cm^{-1}$ represent $E_g$ modes. The second $A_{1g}$ mode appears at 500.1 $cm^{-1}$ in the experimental spectra. An unexpected signal was observed at 661.8 $cm^{-1}$. This signal corresponds to an IR-active mode activated by the disorder and defects from the vibration of the $FeO_4$ tetrahedra.[17] The fact that this signal is much less pronounced in samples prepared at higher substrate temperatures confirms this relation. The intense peak at 1320.3 $cm^{-1}$ originates from second harmonic vibration. The weak and broad peaks at 1041.3 and 1106.1 $cm^{-1}$ were also observed by other authors without further assignment.[17] No other iron oxides aside from hematite, such as maghemite[18] or magnetite[18] were detected, which is in good agreement with the XRD results. Another broad peak at 702.3 $cm^{-1}$ becomes visible for $Fe_2O_3$@Ni-400 in addition to the $\alpha$-$Fe_2O_3$ modes.

This peak originates from the two phonon 2TO modes of the NiO phase. NiO crystallizes in the cubic rock salt structure, therefore no one-phonon modes are expected for perfect crystals but might be activated due to defects. For $Fe_2O_3$@Ni-450, the one-phonon TO and LO mode at 574.6 $cm^{-1}$ and the 2-phonon 2TO mode at 702.3 $cm^{-1}$ from the NiO phase are present. The broad signal at 1400.7 $cm^{-1}$ is attributed to the 2-magnon band.[19]

X-ray photoelectron spectroscopy (XPS) was performed to gain deeper insight into the elemental composition of the surface and the valence states of the respective elements. XPS confirms the presence of iron and oxygen in all deposited films. The Fe 2p high-resolution spectra (Figure 3a) are independent from the substrate temperature and consist of two main peaks for Fe $2p_{3/2}$ and Fe $2p_{1/2}$ with a binding energy difference of 13.4 eV, hence indicating the presence of iron in the oxidation state +III. This assignment is further supported by the characteristic satellite peaks of $Fe^{3+}$ at 710.7 and 724.1 eV. The Ni 2p spectra showed characteristic signals for $Fe_2O_3$@Ni-250 and $Fe_2O_3$@Ni-300, whereas a minor peak was detected at 853.1 eV for $Fe_2O_3$@Ni-350, which may be related to the formation of NiO.

The Ni 2p spectra (Figure 3b) show a characteristic peak at 854.6 eV for $Fe_2O_3$@Ni-400 and $Fe_2O_3$@Ni-450 due to the multiplet splitting of the Ni $2p_{3/2}$ peak, which is typical in the presence of NiO. The peak position and shape of the Ni $2p_{3/2}$ signal are in good agreement with the reported literature values of NiO.[20] Since the characteristic features of metallic nickel were not observed in any of the measurements, we can

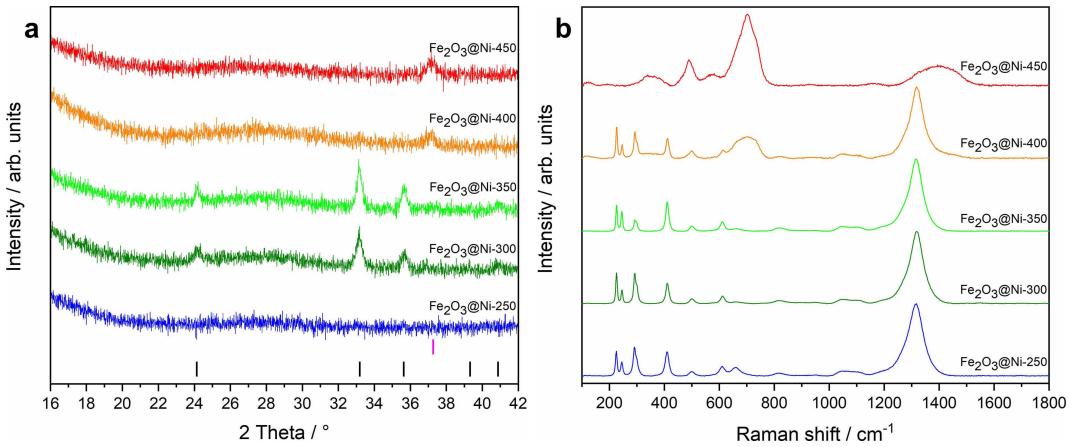


**Figure 2.** XRD patterns of films deposited on Ni foam at different substrate temperatures (a). Only a small range of 2$\theta$ is shown due to the strong reflections from the Ni substrate at 41.5 and 51.8°. The peak positions of the hematite and NiO phase are given as vertical bars in black and purple, respectively. (ICSD#56372 and ICSD#9866). Raman spectra of the films grown at different substrate temperatures (b).

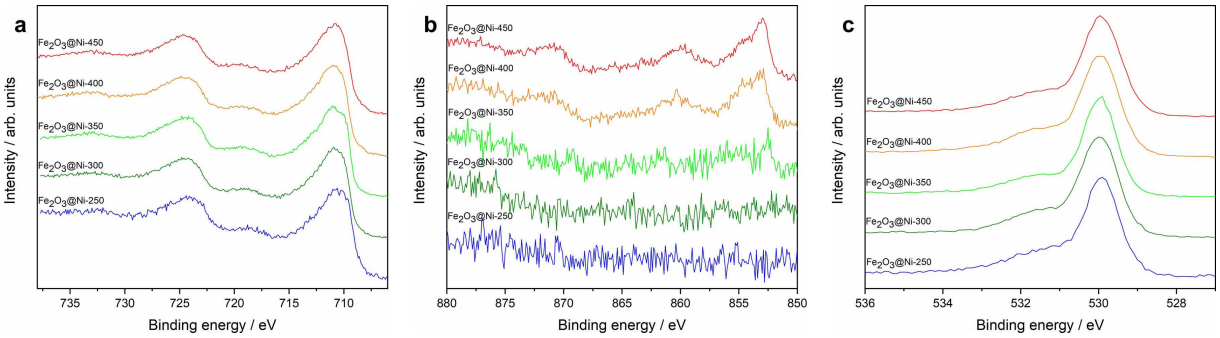


**Figure 3.** XPS core level Fe 2p (a), Ni 2p (b), and O 1 s (c) spectra of films grown on Ni foam at different temperatures before OER.

conclude that the metallic nickel substrate is completely covered with a metal oxide film. The O 1 s spectrum (Figure 3c) consists of two peaks; the peak at lower binding energy (529.4 eV) is associated with the lattice oxygen from α-$Fe_2O_3$ and NiO, however the assignment of the higher binding energy peak at 530.8 eV is rather difficult since several oxygen species due to impurities, defects, and surface adsorbed species are close to each other in this range.

In order to obtain more information on the chemical composition of the α-$Fe_2O_3$ films, time-of-flight secondary ion mass spectrometry (TOF-SIMS) analyses were performed. α-$Fe_2O_3$ films grown on Ni foils under the same previously mentioned conditions were used to avoid undesired influences from the uneven surface of Ni foam. An element-specific mapping (Figure 4e) proved that the films were completely closed, and no discernible holes were observed in the TOF-SIMS analysis at lateral resolution of 3–10 microns (spectrometry

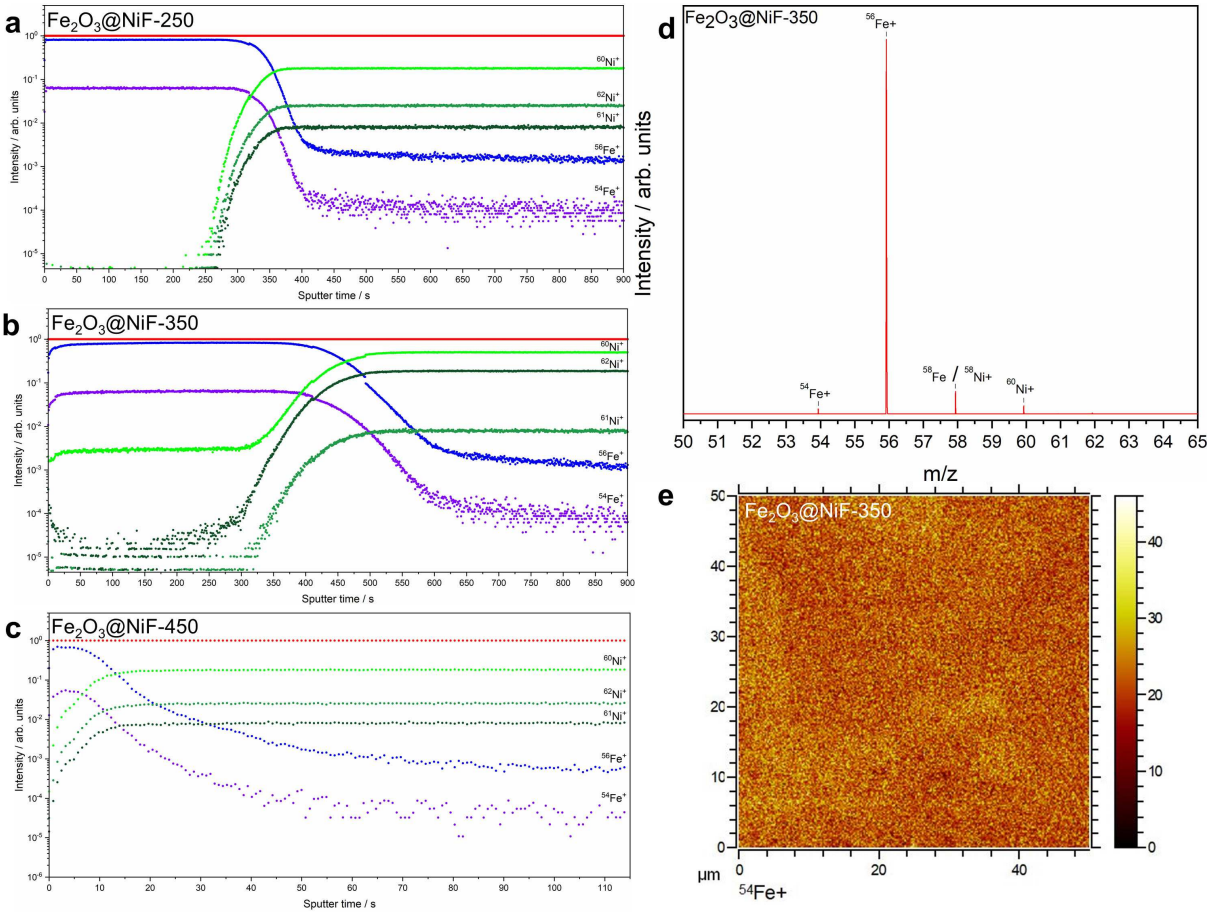


**Figure 4.** TOF-SIMS depth-profile on a α-$Fe_2O_3$ film grown on Ni foil at 250 °C (a), 350 °C (b), and 450 °C (c) under the same conditions as on the Ni foam. TOF-SIMS mass spectra recorded after several sputter cycles (d) and 2D surface map for $^{54}Fe^+$ (e).

mode) and 200 nm (fast imaging mode), respectively. Due to the isobaric mass interference of the most abundant Ni isotope $^{58}Ni^+$ with the iron isotope $^{58}Fe^+$, the less common $^{60}Ni^+$ isotope was chosen for elemental identification. TOF-SIMS depth profiles were recorded using $Bi^+$ ions for $Fe_2O_3$@NiF-250, $Fe_2O_3$@NiF-350, and $Fe_2O_3$@NiF-450 (Figure 4a–c). The film thicknesses for $Fe_2O_3$@NiF-250 and $Fe_2O_3$@NiF-350 are in a comparable range. The depth profile shows that the intensity of all measured iron isotopes is constant over the thickness of the film. Very weak intensities for nickel was found within the film for $Fe_2O_3$@NiF-350. The depth profile measurement was repeated using $Cs^+/Xe^+$ co-sputtering since $MCs^+$ clusters are generally less sensitive to matrix effects than $M^+$ ions for the sample grown at 350 °C. The nickel present in small quantities likely originates from impurities in the $Fe(CO)_5$ precursor. This assumption is supported by the fact that extremely small amounts of other transition metals (e.g., Co and Cu) could also be detected by TOF-SIMS. This is also in good agreement with the results of the XPS analysis, from which no nickel could be detected since the concentration was well below the detection limit. For films grown at higher temperatures, the TOF-SIMS depth profile show a different structure. In these films, the intensity of iron isotopes decreased rapidly after only a few sputtering cycles, while the intensity of nickel isotopes which was already be detected on the surface, increased rapidly. Based on the TOF-SIMS depth-profiles, the thickness of the iron oxide layer, which is almost constant in the temperature window of 250–350 °C, decreases significantly at higher temperatures and is only a few nanometers thick for $Fe_2O_3$@NiF-450. This is in good agreement with the XRD and Raman analyses, which show the formation of NiO in addition to $\alpha$-$Fe_2O_3$ at high temperatures. This behavior is mainly due to the temperature-sensitive iron precursor, which readily decomposes at high temperatures in the reactor feed lines and in the gas phase. In addition, surface poising which can further reduce the thickness of the $\alpha$-$Fe_2O_3$ layer is quite common with this precursor.[21]

### OER characterization

The electrochemical activity of the as-prepared MOCVD grown films on Ni foam was evaluated for the OER by testing them as three-dimensional freestanding working electrodes in a standard three-electrode system with 1 M iron-free KOH as electrolyte at room temperature. The working electrodes were activated before the experiments until stable conditions were reached, while linear sweep voltammograms (LSV) with a scan rate of 5 mV sec$^{-1}$ were recorded of the MOCVD grown films and the bare Ni foam. An anodic peak is observed only in the LSV of the bare Ni foam at 1.39 V vs. reversible hydrogen electrode (RHE) before the OER takes place; this peak corresponds to the oxidation of Ni to a higher oxidation state. The overpotential $\eta$, which is required for a current density of 10 and 50 mA cm$^{-2}$, was used to benchmark the electrocatalysts. The amorphous iron oxide film prepared at 250 °C showed the highest overpotential necessary for a current density of 10 mA cm$^{-2}$ with $\eta_{10}=380$ mV, which is roughly 100 mV lower than the overpotential of bare Ni foam. The overpotential $\eta_{10}$ shows almost no dependency on the chosen substrate temperature during film preparation, where the minimum value for $\eta_{10}=370$ mV was found for the film prepared at 450 °C. The overpotential $\eta_{50}$ necessary for a current density of 50 mA cm$^{-2}$ shows a clearer trend; $\eta_{50}$ decreased with increasing substrate temperature from 520 mV ($Fe_2O_3$@Ni-250) to 420 mV ($Fe_2O_3$@Ni-450). This minimum value is reduced by 250 mV compared to pure nickel foam. To investigate the influence of the Ni substrate, an $\alpha$-$Fe_2O_3$ film on Cu foam was prepared at 300 °C by MOCVD and also characterized as an electrode for the OER. The LSV (Supporting Information, Figure S38) of $Fe_2O_3$@Cu-300 shows with $\eta_{10}=410$ mV an overpotential enhanced by 40 mV compared to $Fe_2O_3$@Ni-300, but due to the steeper rise of the curve, this difference is compensated with $\eta_{50}=460$ mV. With further increasing current density, the OER activity of $Fe_2O_3$@Ni-300 is even outperformed. Figure 5b shows the Tafel plots for the MOCVD grown films, where $\eta$ is plotted against the logarithmic current density log ($j$). The slope of the Tafel plots gives insight into the OER reaction kinetics. A linear behavior of the Tafel slope was found for all of the investigated electrocatalysts. The Tafel slopes for the catalysts are in a narrow range of 55–60 mV dec$^{-1}$ and are significantly lower than the Tafel slope measured for the bare nickel foam.

A Tafel slope in the range of approximately 60 mV dec$^{-1}$ is typically associated with the rate-limiting step during the oxygen evolution.[22] A comparison of the electrochemical OER activity of the MOCVD grown pristine $\alpha$-$Fe_2O_3$ films grown at low temperatures (< 400 °C) with the few iron-only electrocatalysts in the literature shows a significant higher activity than the reported catalysts. (Supporting Information, Table S3). The activity of the pristine $\alpha$-$Fe_2O_3$ films is outperformed by FeNi-based materials with high Ni content, but in these cases, Ni is included in the electrocatalyst, whereas Ni only acts as support for the MOCVD-grown $\alpha$-$Fe_2O_3$ films. The activity reported for NiO in the literature is comparable with the performance of the NiO containing samples grown at high temperatures (> 400 °C). Electrochemical impedance spectra (EIS) were recorded for further insight into the electron transfer kinetics. Figure S37 (Supporting Information) shows the Nyquist plots at an overpotential of 550 mV. The charge-transfer resistance $R_{ct}$ can be extracted from the diameter of the semicircular arc. As seen in Figure S37, the bare Ni foam shows a low charge-transfer resistance of $R_{ct}=11\ \Omega$. The coated foams show slightly higher $R_{ct}$ values in the range of 30–38 Ω, likely due to the expected poor electrical conductivity of $\alpha$-$Fe_2O_3$.

In addition to the overpotential and Tafel slope, the long-term stability of an electrocatalyst is an important factor. To determine this variable, chronopotentiometry measurements were taken at a constant current density of 10 mA cm$^{-2}$ for 12 h. All three examined electrocatalysts, the amorphous $Fe_2O_3$@Ni-250, the crystalline $Fe_2O_3$@Ni-350, and $Fe_2O_3$@Ni-400 show only a very small loss of activity (≈5%), which occurs after a short measuring time. In summary, all catalysts show outstanding long-term stability.

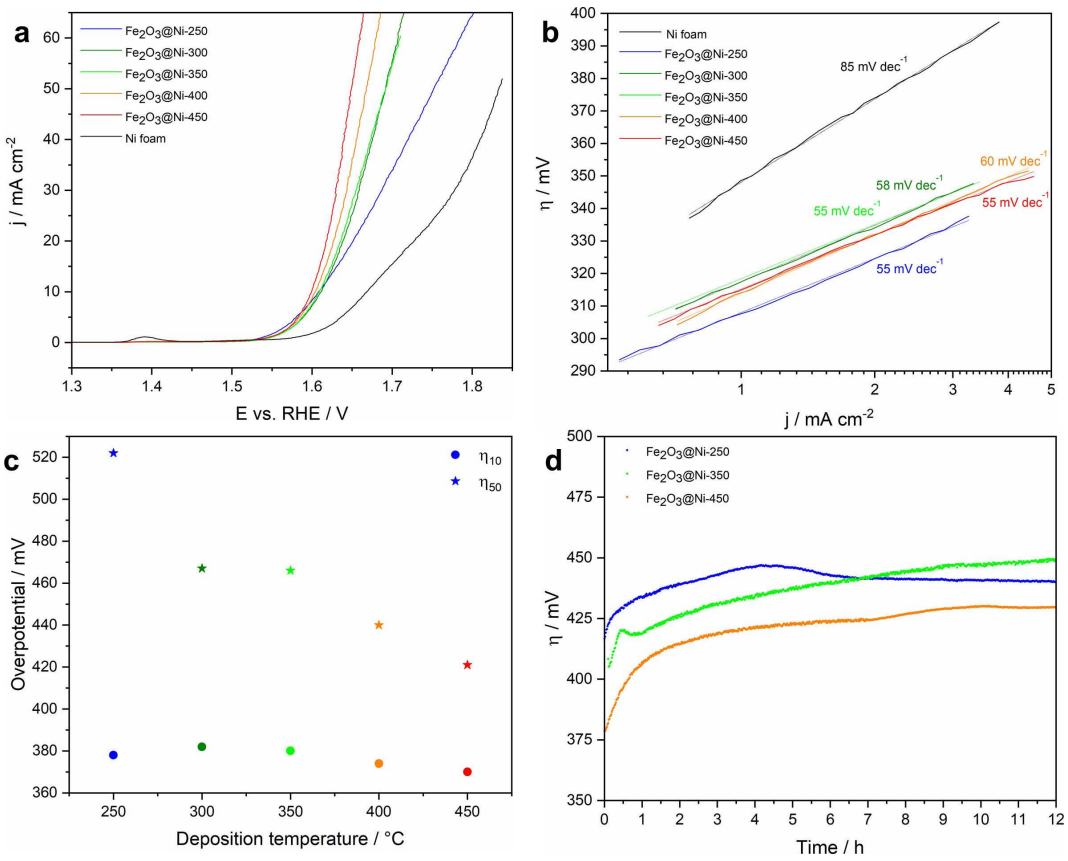


**Figure 5.** LSV (a), Tafel plots (b), overpotentials $\eta_{10}$ and $\eta_{50}$ (c), and chronopotentiometry measurements at a constant current density of 10 mA cm$^{-2}$ (d) of films grown on Ni foam at different temperatures.

### Post-OER characterization

The reaction occurs under harsh conditions, which often lead to chemical or structural changes of the electrocatalyst, hence resulting in its deactivation or destruction. It is therefore necessary crucial to characterize an electrocatalyst both before and after the OER. The iron oxide-coated electrodes show no optically visible changes after the reaction. The SEM photographs (Supporting Information, Figures S7–S11) show that the electrocatalyst film remains intact, where neither cracks nor holes or even peel offs from the electrode surface were observed.

The post catalytic XRD pattern (Figure 6a) exhibits no structural changes in the crystalline phases $\alpha$-$Fe_2O_3$ and NiO, which would otherwise indicate any changes in the lattice parameters or the crystallite size. Similarly, the Raman spectra indicate no changes of the $\alpha$-$Fe_2O_3$ phase in the case of $Fe_2O_3$@Ni-250, $Fe_2O_3$@Ni-300, and $Fe_2O_3$@Ni-350, as well as the $\alpha$-$Fe_2O_3$/NiO phase mixture for $Fe_2O_3$@Ni-400.

In contrast, a new Raman-active mode at 570.2 cm$^{-1}$ was only observed for $Fe_2O_3$@Ni-450 (Figure 6b), which corresponds to the formation of NiOOH, a well-known highly active OER electrocatalyst.[23]

The depth of information from XRD and Raman spectroscopy is only within the micrometer range, while changes as a result of the OER are expected to be limited to only a few nanometers thick of the boundary layer of the electrocatalyst that is in contact with the electrolyte. XPS is an extremely surface-sensitive technique; however, the Fe 2p core level spectrum (Figure 6c) containing the characteristic doublet of Fe $2p_{3/2}$ and Fe $2p_{1/2}$ displays no significant changes caused by the OER. One exception, however, is the film grown at the highest substrate temperature (450 °C). Here the peaks are significantly broadened, which can be explained by the formation of ferric oxyhydroxide FeOOH as a result of the OER. The post-catalytic high-resolution Ni 2p spectrum (Figure 6d) shows a significant change in the Ni $2p_{3/2}$ peak for $Fe_2O_3$@Ni-400 and $Fe_2O_3$@Ni-450 in comparison to the precatalytic state. The change of the peak structure indicates a partial oxidation of $Ni^{2+}$ to $Ni^{3+}$ and thus of the formation of nickel oxyhydroxide on the surface of the catalyst, which is also consistent with the Raman spectra.[24] While the Ni 2p spectrum shows the absence of nickel and nickel oxides in the Ni foams coated at low temperatures before the OER, weak peaks could be observed at 853.8 eV in the post-catalytic state. These can be attributed to NiO, the origin of which is currently unclear but is likely caused by microcracks formed in the electrochemically active layer as a result of the OER. The formation of oxy hydroxides during the OER is also in agreement with the O 1 s spectra (Figure 6e). Compared to the precatalytic state, the intensity of the peak at 530.8 eV is

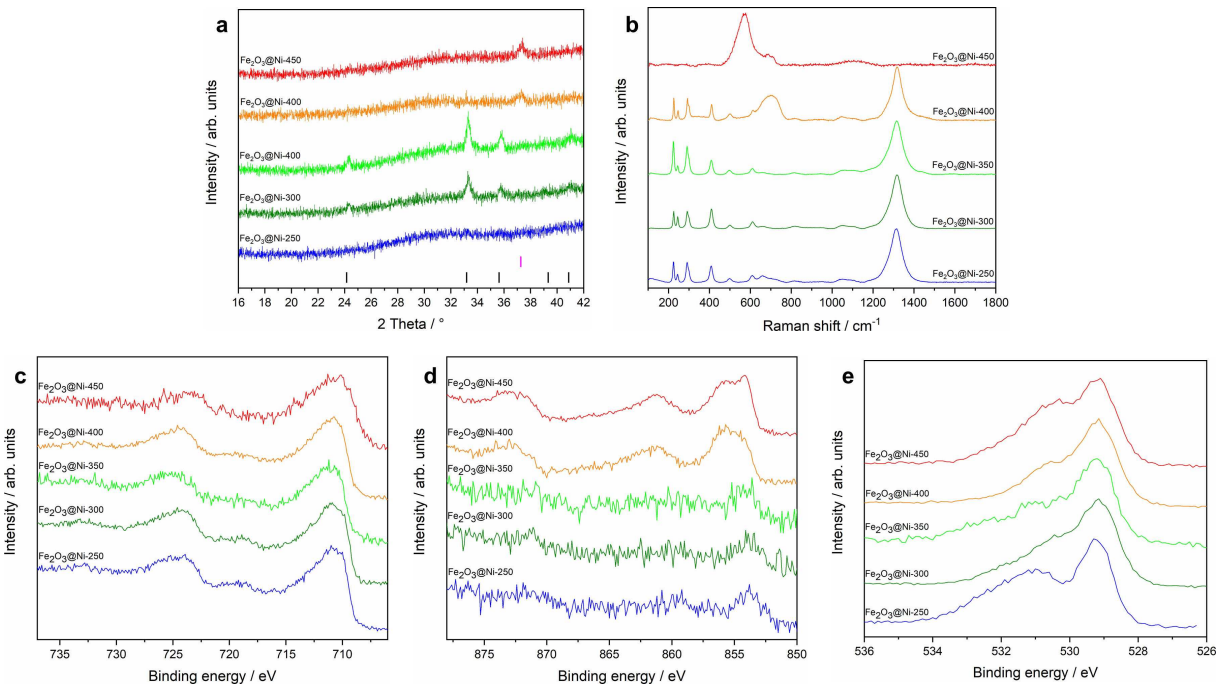


**Figure 6.** XRD patterns (a); Raman spectra (b); XPS core level Fe 2p (c), Ni 2p (d), and O 1 s (e) spectra of films grown on Ni foam at different temperatures after OER.

increased for all samples due the formation of hydroxides and oxy hydroxides during the OER.

## Conclusions

Three-dimensional electrodes for the oxygen evolution reaction (OER) have been successfully fabricated by the direct growth of iron oxide on Nickel foam in a metalorganic chemical vapor deposition (MOCVD) process using $Fe(CO)_5$ as CVD precursor. The formation of amorphous $\alpha$-$Fe_2O_3$ was observed at a low substrate temperature (250 °C), whereas crystalline $\alpha$-$Fe_2O_3$ was formed at higher temperatures. Above 350 °C, the $\alpha$-$Fe_2O_3$ films partially incorporates crystalline NiO. The deposited electrochemical active films are free of organic binders as well as noble and toxic metals. The OER performances of the MOCVD-grown films on Nickel foam as support were evaluated by measuring the overpotential required to generate a current of 10 and 50 mA cm$^{-2}$. The respective Tafel slopes and long-term stability were also determined. At low temperatures (250–350 °C), the resulting $\alpha$-$Fe_2O_3$ films show high activity in the OER for iron oxide-based catalysts, an overpotential $\eta_{50}$ reduced by 160 mV, and finally a lower Tafel slope compared to bare nickel foam. The Ni foam was successfully replaced by Cu foam ($Fe_2O_3$@Cu-300), which demonstrated that the high electrochemical activity of MOCVD-grown pristine $\alpha$-$Fe_2O_3$ is independent of the metallic support and that Ni is not required for high electrocatalytic performance. The electrodes coated at higher temperatures show even lower overpotentials [$\eta_{50}$ = 440 mV ($Fe_2O_3$@Ni-400) and 420 mV ($Fe_2O_3$@Ni-450)]; however, the high electrochemical activity originates from the formation of nickel oxyhydroxides in the NiO layer rather from the iron species.

## Experimental Section

### Synthetic procedures, materials, and methods

The nickel foams and nickel sheets were treated with diluted hydrochloric acid for 10 min in an ultrasonic bath in order to remove the native oxide layer before use. To remove the hydrochloric acid from the surface, they were ultrasonically treated in distilled water for another 10 min. Finally, the foams and sheets were rinsed with acetone and dried at room temperature. Iron pentacarbonyl was obtained from Sigma-Aldrich und used without further purification.

The MOCVD growth of iron oxide was performed in a cold-wall low-pressure MOCVD reactor described elsewhere.[25] $Fe(CO)_5$ was used as iron precursor with dried Argon as carrier gas (3 sccm) and a mixture of Argon (68 sccm) and air (12 sccm) as oxidizer. Cleaned Ni foam or sheets were used as substrate. Material films were deposited within 30 min at a working pressure of 500 mbar. After the film deposition was complete, the system was cooled to ambient temperature within 30 min under vacuum.

### Characterization

XRD patterns were measured using a Bruker D8 Advance powder diffractometer with Cu$K_\alpha$ radiation with $\lambda$ = 1.5418 Å.

XPS was performed using a Versaprobe II™ from Ulvac-Phi with monochromatic Al$K_\alpha$ light at 1486.6 eV photon energy. The emission angle between analyzer and sample was 45°.

The surface morphology of the iron oxide film was investigated by SEM using an Apreo S LoVac equipped with an EDX device and AFM using a Nanosurf NaioAFM.

The TOF-SIMS experiments were preformed using a TOF.SIMS 5 from IONTOF equipped with a $Bi^+$ primary ion gun for analysis. For depth-profiling, this machine is equipped with an $O_2^+$ and a $Cs^+$/$Xe^+$ ion source for sputtering. The measurements were performed using a $Bi^+$ primary beam at 30 kV and $100\times100\ \mu m^2$ operated in spectrometry mode and an $O_2^+$ or $Cs^+$/$Xe^+$ sputter beam at 2 kV and $300\times300\ \mu m^2$ operated in non-interlaced sputtering mode. A flood gun and gas flooding at an oxygen pressure of $2\cdot10^{-6}$ mbar were used in order to compensate sample charging effects.

The electrochemical measurements were performed in a three-electrode cell using an Autolab potentiostat/galvanostat. The coated Ni foam was used as working electrode, Ag/AgCl/3 M KCL as reference electrode and platinum mesh as counter electrode. 1 M KOH (iron-free, SigmaAldrich) with pH = 14 was used as electrolyte. The measured potentials were converted to the RHE scale using the following equation $E_{RHE} = E_{Ag/AgCl} + 0.210\ V + 0.059\ pH$. EIS was then recorded in the frequency range from 50 kHz to 1 Hz at the corresponding open circuit potential of the electrode, using an AC perturbation of 10 mV. The resistance of the solution was determined from the resulting Nyquist plot, and the latter used for ohmic drop correction according to the relation, $E_c = E_m - iR$, where $E_c$ is the corrected potential, $E_m$ is the applied potential and $iR$ is the ohmic drop.

## Acknowledgements

*G.B is thankful for funding by the "Programm zur Förderung des exzellenten wissenschaftlichen Nachwuchses" from the University Duisburg-Essen. Support by the Interdisciplinary Center for Analytics on the Nanoscale (ICAN) of the University of Duisburg-Essen, a DFG funded core facility (DFG RIsources reference: RI_00313), is gratefully acknowledged (XPS and TOF-SIMS measurements, service operation). Open access funding enabled and organized by Projekt DEAL.*

## Conflict of Interest

The authors declare no conflict of interest.

**Keywords:** iron oxide · MOCVD · sustainable chemistry · thin films · water splitting

[1] S. Trasatti, *J. Electroanal. Chem.* **1999**, *476*, 90–91.
[2] C. Hu, L. Zhang, J. Gong, *Energy Environ. Sci.* **2019**, *12*, 2620–2645.
[3] X. Li, X. Hao, A. Abudula, G. Guan, *J. Mater. Chem. A* **2016**, *4*, 11973–12000.
[4] X. Xu, Z. Zhong, X. Yan, L. Kang, J. Yao, *J. Mater. Chem. A* **2018**, *6*, 5999–6006.
[5] B. Sidhureddy, J. S. Dondapati, A. Chen, *Chem. Commun.* **2019**, *55*, 3626–3629.
[6] A. Mendoza-Garcia, D. Su, S. Sun, *Nanoscale* **2016**, *8*, 3244–3247.
[7] X. Ma, W. Zhang, Y. Deng, C. Zhong, W. Hu, X. Han, *Nanoscale* **2018**, *10*, 4816–4824.
[8] E. A. Schultz-Sikma, H. M. Joshi, Q. Ma, K. W. MacRenaris, A. L. Eckermann, V. P. Dravid, T. J. Meade, *Chem. Mater.* **2011**, *23*, 2657–2664.
[9] H. A. Bandal, A. R. Jadhav, A. A. Chaugule, W. J. Chung, H. Kim, *Electrochim. Acta* **2016**, *222*, 1316–1325.
[10] P. Sharma, J. W. Jang, J. S. Lee, *ChemCatChem* **2019**, *11*, 157–179.
[11] J. Liu, H. Yuan, Z. Wang, J. Li, M. Yang, L. Cao, G. Liu, D. Qian, Z. Lu, *Chem. Commun.* **2019**, *55*, 10860–10863.
[12] N. Dalai, B. Mohanty, A. Mitra, B. Jena, *ChemistrySelect* **2019**, *4*, 7791–7796.
[13] S. Lee, K. Banjac, M. Lingenfelder, X. Hu, *Angew. Chem. Int. Ed.* **2019**, *58*, 10295–10299; *Angew. Chem.* **2019**, *131*, 10401–10405.
[14] a) X. Xu, Z. Zhong, X. Yan, L. Kang, J. Yao, *J. Mater. Chem. A* **2018**, *6*, 5999–6006; b) S. H. Ahn, A. Manthiram, *J. Mater. Chem. A* **2017**, *5*, 2496–2503; c) S. H. Bae, J. E. Kim, H. Randriamahazaka, S. Y. Moon, J. Y. Park, I. K. Oh, *Adv. Energy Mater.* **2017**, *7*, 1–11.
[15] J. S. Sagu, D. Mehta, K. G. U. Wijayantha, *Electrochem. Commun.* **2018**, *87*, 1–4.
[16] a) N. Weidler, S. Paulus, J. Schuch, J. Klett, S. Hoch, P. Stenner, A. Maljusch, J. Brötz, C. Wittich, B. Kaiser, W. Jaegermann, *Phys. Chem. Chem. Phys.* **2016**, *18*, 10708–10718; b) N. Weidler, J. Schuch, F. Knaus, P. Stenner, S. Hoch, A. Maljusch, R. Schäfer, B. Kaiser, W. Jaegermann, *J. Phys. Chem. C* **2017**, *121*, 6455–6463.
[17] a) D. Bersani, P. P. Lottici, A. Montenero, *J. Raman Spectrosc.* **1999**, *30*, 355–360; b) Y. Y. Xu, D. Zhao, X. J. Zhang, W. T. Jin, P. Kashkarov, H. Zhang, *Physica E Low Dimens. Syst. Nanostruct.* **2009**, *41*, 806–811.
[18] D. L. A. De Faria, S. Venâncio Silva, M. T. De Oliveira, *J. Raman Spectrosc.* **1997**, *28*, 873–878.
[19] N. Mironova-Ulmane, A. Kuzmin, I. Steins, J. Grabis, I. Sildos, M. Pärs, *J. Phys. Conf. Ser.* **2007**, *93*, 8–13.
[20] I. Preda, A. Gutiérrez, M. Abbate, F. Yubero, J. Méndez, L. Alvarez, L. Soriano, *Phys. Rev. B* **2008**, *77*, 1–7.
[21] P. Zhang, E. Mohimi, T. K. Talukdar, J. R. Abelson, G. S. Girolami, *J. Vac. Sci. Technol. A* **2016**, *34*, 051518.
[22] N. T. Suen, S. F. Hung, Q. Quan, N. Zhang, Y. J. Xu, H. M. Chen, *Chem. Soc. Rev.* **2017**, *46*, 337–365.
[23] L. F. Li, Y. F. Li, Z. P. Liu, *ACS Catal.* **2020**, *10*, 2581–2590.
[24] A. P. Grosvenor, M. C. Biesinger, R. S. C. Smart, N. S. McIntyre, *Surf. Sci.* **2006**, *600*, 1771–1779.
[25] G. Bendt, S. Schulz, S. Zastrow, K. Nielsch, *Chem. Vap. Deposition* **2013**, *19*, 235–241.

Manuscript received: August 7, 2020
Revised manuscript received: September 10, 2020
Accepted manuscript online: September 14, 2020
Version of record online: September 30, 2020